SAND2023-08132J

International Journal of Fracture manuscript No.
(will be inserted by the editor)

Identifying crack tip position and stress intensity factors from displacement data

Swati Gupta · Grant West · Mark A. Wilson · Scott J. Grutzik · Derek H. Warner

International Journal of Fracture

Abstract Fracture prognosis and characterization efforts require knowledge of crack tip position and the configurational driving force acting on the crack. Here, we present an efficient numerical approach to infer both of these characteristics under a consistent theoretical framework from noisy, unstructured displacement data. The novel approach utilizes the separability of the asymptotic linear elastic fracture mechanics fields to expedite the search for crack tip position and is particularly useful for noisy displacement data. The manuscript begins with an assessment of the importance of accurately locating crack tip position when quantifying the crack driving force from displacement data. Next, the proposed separability approach for quickly inferring crack tip position is introduced. Comparing to the widely used displacement correlation approach, the performance of the separability approach is assessed. Cases involving both noisy data and systematic deviation from the asymptotic linear elastic fracture mechanics model are considered, e.g. inelastic material behavior and finite geometries. An open source python implementation of the proposed approach is available for use by those doing field and laboratory work involving digital image correlation and simulations, e.g. finite element, discrete element, molecular dynamics and peridynamics, where the crack tip position is not explicitly defined.

1 Introduction

Fracture prognosis and characterization efforts require knowledge of crack tip position and the configurational driving force acting on the crack. In many cases, the two tasks are related, as the crack tip position is a necessary input for identifying the driving force. In the limit of scale separation, e.g. crack tip process

Swati Gupta
Cornell Fracture Group, School of Civil and Environmental Engineering, Cornell University, Ithaca NY 14853, USA

Grant West
Cornell Fracture Group, School of Civil and Environmental Engineering, Cornell University, Ithaca NY 14853, USA

Mark A. Wilson
Sandia National Laboratories, Computational Materials and Data Science, Albuquerque NM 87123, USA

Scott J. Grutzik
Sandia National Laboratories, Materials and Failure Modeling, Albuquerque NM 87123, USA

Derek H. Warner
Cornell Fracture Group, School of Civil and Environmental Engineering, Cornell University, Ithaca NY 14853, USA
E-mail: derek.warner@cornell.edu

zone ≪ crack size ≪ specimen size, ambiguities in the definition of crack tip position are not significant. However in reality, scale separation is often difficult to achieve and the definition of the crack tip position may impact the inference of crack driving force.

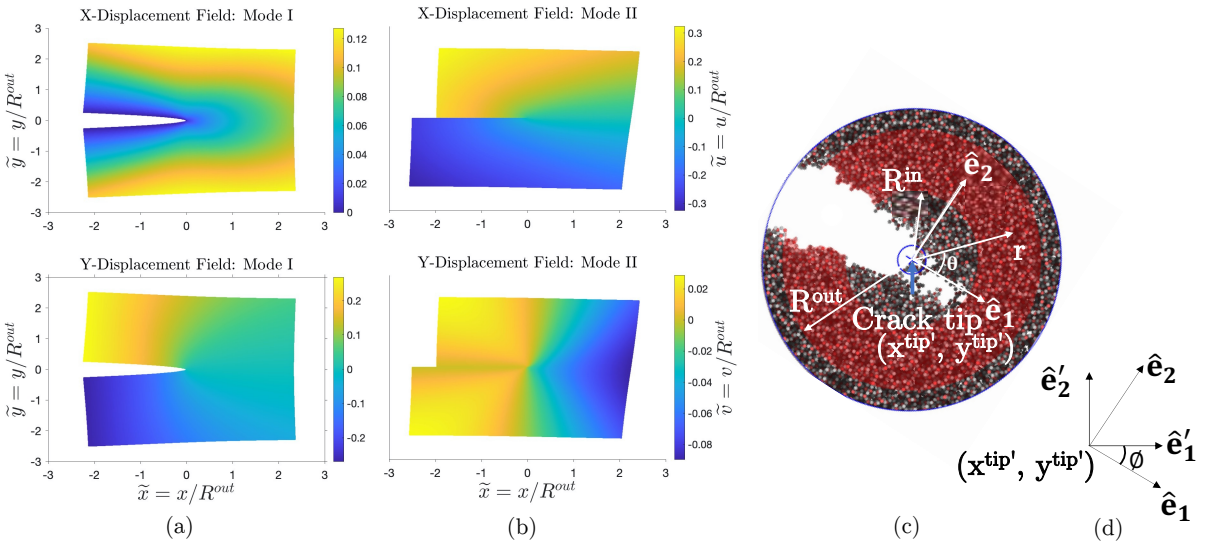

Fig. 1 The displacement fields in the x and y directions for (a) mode I and (b) mode II loading. Configurational details demonstrating (c) the crack tip relationships with the local coordinate system, centered and aligned with the crack tip, and the annulus of K-dominance with inner radius R^{in} and outer radius R^{out}. (d) The global coordinate system with basis vectors $\hat{e}_1^{'}$ and $\hat{e}_2^{'}$, showing the crack tip position, $(x^{tip'}, y^{tip'})$.

Crack tip position can be defined geometrically or mechanically. When the characterization of crack driving force is a goal, it is sensible to define crack tip position using the mechanical field (i.e. displacement). This can be problematic in that the definition of crack tip position with respect to the mechanical field is ambiguous. For example, one might define the crack tip position to be the forward most location where no stress is transferred across the fracture plane, or the location where the maximum stress is transferred, or something different. In this manuscript, we advocate that a mechanical definition of crack tip position should be consistent with the model used for inferring the crack driving force. In the ubiquitous case of linear elastic fracture mechanics (LEFM) (Zehnder, 2012), this equates to choosing a crack tip position that maximizes the correspondence between a given data set and the LEFM model within an annulus centered about the crack tip. This approach is widely applicable, where the "given data set" can represent field or laboratory measurements of displacements at a set of points (e.g. digital image correlation) or the calculation of displacements at a set of points via computer simulations, e.g. finite element or molecular dynamics modeling.

In the LEFM model, the distribution of stresses in the vicinity of a sharp crack tip determine the configurational driving force. The distribution of near tip stresses is completely characterized by the three independent stress intensity factors, K_I, K_{II}, and K_{III}, and a constant background stress known as the T-stress, T. The three stress intensity factors correspond to the opening, sliding, and tearing modes of deformation, respectively. The T-stress is often disregarded, but it can play a significant role in some cases and is thus included here (Ayatollahi and Nejati, 2011; Rice, 1974; Smith et al., 2001; Stepanova and Roslyakov, 2016; Suresh, 1998). For brevity, attention will be restricted to 2D problems involving an

elastically isotropic linear material undergoing the opening and sliding modes, noting that extension to cases involving out-of-plane tearing or elastic anisotropy would be straightforward.

With the stress field not being observable, we focus on the associated displacement field, which can be expressed as

$$\begin{bmatrix} u(\boldsymbol{r},\boldsymbol{\mu},\boldsymbol{K}) \\ v(\boldsymbol{r},\boldsymbol{\mu},\boldsymbol{K}) \end{bmatrix} = \begin{bmatrix} \sqrt{r}f_1(\boldsymbol{\mu},\theta) & \sqrt{r}f_2(\boldsymbol{\mu},\theta) & rf_3(\boldsymbol{\mu},\theta) \\ \sqrt{r}g_1(\boldsymbol{\mu},\theta) & \sqrt{r}g_2(\boldsymbol{\mu},\theta) & rg_3(\boldsymbol{\mu},\theta) \end{bmatrix} \begin{bmatrix} K_I \\ K_{II} \\ T \end{bmatrix} \tag{1}$$

with

$$\begin{bmatrix} f_1(\boldsymbol{\mu},\theta) \\ f_2(\boldsymbol{\mu},\theta) \\ f_3(\boldsymbol{\mu},\theta) \\ g_1(\boldsymbol{\mu},\theta) \\ g_2(\boldsymbol{\mu},\theta) \\ g_3(\boldsymbol{\mu},\theta) \end{bmatrix} = \frac{1}{2\mu} \begin{bmatrix} \sqrt{\frac{1}{2\pi}}((\kappa-\frac{1}{2})\cos\frac{\theta}{2} - \frac{1}{2}\cos\frac{3\theta}{2}) \\ \sqrt{\frac{1}{2\pi}}((\kappa+\frac{3}{2})\sin\frac{\theta}{2} + \frac{1}{2}\sin\frac{3\theta}{2}) \\ \frac{1}{4}(\kappa+1)\cos\theta \\ \sqrt{\frac{1}{2\pi}}((\kappa+\frac{1}{2})\sin\frac{\theta}{2} - \frac{1}{2}\sin\frac{3\theta}{2}) \\ \sqrt{\frac{1}{2\pi}}((\kappa-\frac{3}{2})\cos\frac{\theta}{2} + \frac{1}{2}\cos\frac{3\theta}{2}) \\ \frac{1}{4}(\kappa-3)\sin\theta \end{bmatrix} \tag{2}$$

relative to a local coordinate system centered and aligned with the crack tip, having basis vectors $\hat{e}_1$ and $\hat{e}_2$, as depicted in Figure 1 (Williams, 1957). In Equation (1), r represents the distance from the crack tip and θ represents the angle relative to the $\hat{e}_1$ basis vector, which lies in the plane of the crack. To compactly illustrate functional dependencies, we use the bold characters $\boldsymbol{r} = [r, \theta]$, $\boldsymbol{\mu} = [\mu, \kappa]$, and $\boldsymbol{K} = [K_I, K_{II}, T]$.

We will consider the elastic constants to be known (μ the shear modulus and κ the Kolosov constant) $\kappa = (3-\nu)/(1+\nu)$ for plane stress condition and $\kappa = 3-4\nu$ for plane strain (ν is Poisson's ratio). Thus, the LEFM model displacement field Equation (1)) depends on six parameters: crack tip position, $x^{tip'}$ and $y^{tip'}$, orientation of the crack tip, ϕ', and K_I, K_{II}, and T. $x^{tip'}$, $y^{tip'}$ and ϕ' are described relative to a global coordinate system with basis vectors $\hat{e}'_1$ and $\hat{e}'_2$ (Figure 1). Hence, the identification of the crack tip position and driving force from observed displacement data can then be viewed as a single nonlinear minimization/optimization problem, whereby the discrepancy between the given displacement data set and the asymptotic LEFM displacement field within an annulus is minimized over these six parameters. To assess the discrepancy between the given data set and the asymptotic LEFM field, a displacement data point i, observed in the global coordinate system at x'_i and y'_i and having displacement components of $u_i^{obs'}$ and $v_i^{obs'}$, can be expressed relative to Equation (1) via a rigid transformation

$$\begin{bmatrix} u_i^{obs}(\phi') \\ v_i^{obs}(\phi') \end{bmatrix} = \begin{bmatrix} \cos\phi' & \sin\phi' \\ -\sin\phi' & \cos\phi' \end{bmatrix} \begin{bmatrix} u_i^{obs'} \\ v_i^{obs'} \end{bmatrix} \tag{3}$$

and

$$\begin{bmatrix} r_i^{obs}(\phi', \boldsymbol{x'_i}, \boldsymbol{x^{tip'}}) \\ \theta_i^{obs}(\phi', \boldsymbol{x'_i}, \boldsymbol{x^{tip'}}) \end{bmatrix} = \begin{bmatrix} \cos\phi' & \sin\phi' \\ -\sin\phi' & \cos\phi' \end{bmatrix} \begin{bmatrix} x'_i - x^{tip'} \\ y'_i - y^{tip'} \end{bmatrix}, \tag{4}$$

where the position of the crack tip in the global coordinate system is expressed compactly as $\boldsymbol{x^{tip'}} = \left[x^{tip'}, y^{tip'}\right]$ while the coordinates of a particular data point i in the given data set are presented as $\boldsymbol{x'_i} = \left[x'_i, y'_i\right]$. In addition to aligning coordinate systems, this transformation will also remove any in-plane

rigid body motions that might exist in the given displacement data set. The left side of Equation (4) will be subsequently represented in compact form as $\boldsymbol{r_i^{obs}}(\phi', \boldsymbol{x_i'}, \boldsymbol{x^{tip'}})$.

The discrepancy between the LEFM model and a given data point i is quantified with a residual vector,

$$\begin{bmatrix} \mathfrak{R}_i^u \\ \mathfrak{R}_i^v \end{bmatrix} = \begin{bmatrix} u_i^{obs}(\phi') - u(\boldsymbol{r}_i^{obs}(\phi', \boldsymbol{x_i'}, \boldsymbol{x^{tip'}}), \boldsymbol{\mu}, \boldsymbol{K}) \\ v_i^{obs}(\phi') - v(\boldsymbol{r}_i^{obs}(\phi', \boldsymbol{x_i'}, \boldsymbol{x^{tip'}}), \boldsymbol{\mu}, \boldsymbol{K}) \end{bmatrix}. \tag{5}$$

Subsequently, the 6 model parameters $\boldsymbol{x^{tip'}}$, ϕ', and $\boldsymbol{K}$ that minimize the residual vector's normalized length across the data set with n number of data points,

$$\Phi^{dc} = \frac{1}{n} \sum_{i=1}^{n} \left((\mathfrak{R}_i^u)^2 + (\mathfrak{R}_i^v)^2 \right), \tag{6}$$

is the best fit LEFM model in terms of a least squares measure when the elastic constants $\boldsymbol{\mu}$ are known.

When $\boldsymbol{x}^{tip'}$ and ϕ' are prescribed to be fixed values, the minimization of Φ^{dc} simplifies to a linear regression problem, as detailed in Wilson et al. (2019). Numerous examples of this case are found throughout the literature (Ayatollahi and Nejati, 2011; Lim et al., 1992; Sanford and Dally, 1979; Seitl et al., 2017).

In this manuscript, we present an approach for the nonlinear problem of identifying crack tip position when $\boldsymbol{x}^{tip'}$ and ϕ' are not prescribed. The approach utilizes the separable characteristic of the asymptotic LEFM displacement field to accelerate the computation of crack tip position by avoiding a minimization over the six unknown parameters of Equation (6). Following a search for the crack tip position with the proposed separability approach, a single nonlinear optimization problem over ϕ', K_I, K_{II}, and T can be performed at that crack tip position to identify the driving force.

The manuscript begins with an assessment of the implications of inaccurately locating crack tip position for the purpose of quantifying the driving force from a given displacement data set. Then, the proposed approach is presented and its performance across a range of applications is examined. The proposed approach presented here will be subsequently referred to as the "separability approach". The widely used regression approach described by Equations (3)-(6) will be referred to as the "displacement correlation approach".

2 Role of Crack Tip Position in the Computation of Stress Intensity Factors

The role of the crack tip position in the determination of the stress intensity factors is illustrated here with a simple example. To highlight the universality of the results presented in this and subsequent sections, the stress intensity factors are presented in units of $\mu\sqrt{R^{out}}$, where μ is the shear modulus of the material. R^{out} is the outer radius of an annulus centered at the crack tip and is the only length scale of the problem. Hence, all length scales are represented in units of R^{out}. The normalized variables are denoted using a tilde, e.g. $\widetilde{u} = u/R^{out}$, $\widetilde{r} = r/R^{out}$, and $\widetilde{K_I} = K_I/\mu\sqrt{R^{out}}$.

To highlight the importance of the assumed crack tip for correctly computing stress intensity factors, a synthetic infinite medium mode I displacement field was created with a known position of the crack tip at (0,0). A collection of 250,000 points was placed as a regular grid within a square domain of length $25R^{out}$ thereby arranged in a grid spacing of $L = 0.05R^{out}$. The example presented here (Figure 2) corresponds to synthetic displacement data generated from Equation (1) with $\widetilde{K_I} = 1.10$, $\widetilde{K_{II}} = 0.00$ and $\widetilde{T} = 0.00$. The annulus was centered on the presumed crack tip, with R^{in} chosen to be $0.1R^{out}$, and it encompassed 1240 points. Points lying within a distance of 1.5 R^{out} of the true crack tip position, in both x and y directions, were used as potential crack tip positions. The associated K_I value, K_I^{infer}, was inferred using Equation (1) for each of these potential crack tip positions. In order to compute errors in the inferred K_I values, the K_I value associated with $\widetilde{K_I} = 1.10$ was considered as the ground truth and this value is referred to as K_I^{true}. The errors between K_I^{true} and K_I^{infer} for each assumed crack tip position are plotted in Figure 2.

Figure 2 demonstrates that inaccuracy due to an incorrectly assumed crack tip position can lead to both over and under predictions of K_I, dependent upon the relative location of the assumed position. This was found to be true for K_{II} as well, though it has not been shown here for the sake of brevity. With respect to the goal of locating the crack tip, Figure 2 demonstrates that a search seeking to maximize or minimize configurational driving forces such as K_I will not suffice to identify the crack tip position. Further, the values of stress intensity that are computed at an incorrect crack tip position do not bound the true value.

For K_I, the error nears its maximum along the crack propagation direction $\hat{e}_1$, where it scales approximately linearly with distance below $0.5R^{out}$. This motivates the choice of using a maximally sized annulus when inferring K_I to minimize error arising from an incorrectly assumed or inferred crack tip position.

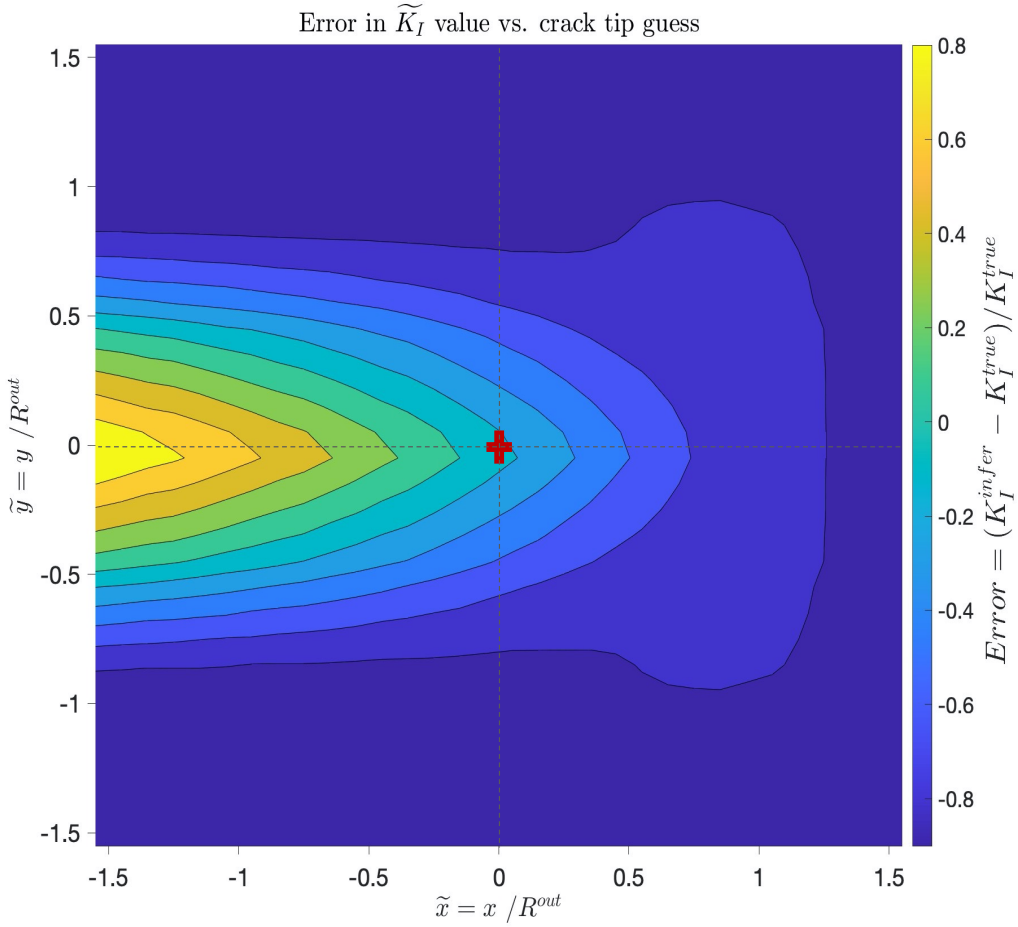

Fig. 2 Errors between actual K_I values (K_I^{true}) for a square domain with $\widetilde{K_I} = 1.10$, $\widetilde{K_{II}} = 0.00$, $\widetilde{T} = 0.00$ and the inferred K_I values (K_I^{infer}) computed as a function of assumed crack tip position. The actual crack tip is marked with a '+' sign and located at (0,0), where the error is zero as indicated by the color bar on the right.

3 Inferring Crack Tip Position

Having established the importance of accurately locating the crack tip position, we now propose an approach to expedite the inference of the crack tip position. The proposed approach is referred to as the "separability approach," as it exploits the multiplicative separability of the asymptotic near tip stress field into radial and angular components. It will be shown to be effective even when substantial noise exists in the observed displacements.

To begin, the separability approach considers the expected value of each component of the displacement field within a sub-annulus j, where the inner radius of this sub-annulus j is defined as $R_j^{in} = \frac{j}{m}\left(R^{out} - R^{in}\right)$ for a total number of m sub-annuli. The outer radius of the sub-annulus j is a multiple of the inner radius, i.e. $R_j^{out} = \alpha R_j^{in}$, where $\alpha \in \mathbb{R}^+$. From Equation (1), this is expressed as

$$\begin{bmatrix} \overset{j}{E}\left[u(\boldsymbol{r},\theta)\right] \\ \overset{j}{E}\left[v(\boldsymbol{r},\theta)\right] \end{bmatrix} = \begin{bmatrix} \overset{j}{E}\left[\sqrt{\boldsymbol{r}}\right]\overset{j}{E}\left[f_1(\boldsymbol{\mu},\theta)\right] & \overset{j}{E}\sqrt{\boldsymbol{r}}\right]\overset{j}{E}\left[f_2(\boldsymbol{\mu},\theta)\right] & \overset{j}{E}\left[\boldsymbol{r}\right]\overset{j}{E}\left[f_3(\boldsymbol{\mu},\theta)\right] \\ \overset{j}{E}\left[\sqrt{\boldsymbol{r}}\right]\overset{j}{E}\left[g_1(\boldsymbol{\mu},\theta)\right] & \overset{j}{E}\left[\sqrt{\boldsymbol{r}}\right]\overset{j}{E}\left[g_2(\boldsymbol{\mu},\theta)\right] & \overset{j}{E}\left[\boldsymbol{r}\right]\overset{j}{E}\left[g_3(\boldsymbol{\mu},\theta)\right] \end{bmatrix} \begin{bmatrix} K_I \\ K_{II} \\ T \end{bmatrix} \tag{7}$$

where the linearity of the expectation operator $\overset{j}{E}$ in the sub-annulus j allows the expectation to be applied independently to each entry in the 2x3 matrix, and the separable nature of each entry allows the expectation to be applied over r and θ independently. The form of the θ dependent terms and the range of the expectation, $[-\pi, \pi]$, produces zeros in 4 of the 6 components, reducing Equation (7) to

$$\begin{bmatrix} \overset{j}{E}\left[u(\boldsymbol{r},\theta)\right] \\ \overset{j}{E}\left[v(\boldsymbol{r},\theta)\right] \end{bmatrix} = \begin{bmatrix} \overset{j}{E}\left[\sqrt{\boldsymbol{r}}\right]\overset{j}{E}\left[f_1(\boldsymbol{\mu},\theta)\right] & 0 & 0 \\ 0 & \overset{j}{E}\left[\sqrt{\boldsymbol{r}}\right]\overset{j}{E}\left[g_2(\boldsymbol{\mu},\theta)\right] & 0 \end{bmatrix} \begin{bmatrix} K_I \\ K_{II} \\ T \end{bmatrix} \tag{8}$$

For all observed data points having positions within a sub-annulus j, the average displacement components are denoted as $\overline{\overset{j}{u_i^{obs}}}$ and $\overline{\overset{j}{v_i^{obs}}}$, respectively. Accordingly, $\overline{\overset{j}{u_i^{obs}}}$ and $\overline{\overset{j}{v_i^{obs}}}$ can be viewed as approximations of $\overset{j}{E}\left[u\right]$ and $\overset{j}{E}\left[v\right]$ with residuals $\overline{\overset{j}{\mathfrak{R}_i^u}}$ and $\overline{\overset{j}{\mathfrak{R}_i^v}}$. From this vantage, Equation (7) can be utilized to write

$$\begin{bmatrix} \overline{\overset{j}{u_i^{obs}}} \\ \overline{\overset{j}{v_i^{obs}}} \end{bmatrix} = \begin{bmatrix} \overset{j}{E}\left[\sqrt{\boldsymbol{r}}\right]\overset{j}{E}\left[f_1(\boldsymbol{\mu},\theta)\right] & 0 & 0 \\ 0 & \overset{j}{E}\left[\sqrt{\boldsymbol{r}}\right]\overset{j}{E}\left[g_2(\boldsymbol{\mu},\theta)\right] & 0 \end{bmatrix} \begin{bmatrix} K_I \\ K_{II} \\ T \end{bmatrix} + \begin{bmatrix} \overline{\overset{j}{\mathfrak{R}_i^u}} \\ \overline{\overset{j}{\mathfrak{R}_i^v}} \end{bmatrix}, \tag{9}$$

which reduces to

$$\begin{bmatrix} \overline{\overset{j}{u_i^{obs}}} \\ \overline{\overset{j}{v_i^{obs}}} \end{bmatrix} = \begin{bmatrix} K_I\ \overset{j}{E}\left[\sqrt{\boldsymbol{r}}\right]\overset{j}{E}\left[f_1(\boldsymbol{\mu},\theta)\right] \\ K_{II}\ \overset{j}{E}\left[\sqrt{\boldsymbol{r}}\right]\overset{j}{E}\left[g_2(\boldsymbol{\mu},\theta)\right] \end{bmatrix} + \begin{bmatrix} \overline{\overset{j}{\mathfrak{R}_i^u}} \\ \overline{\overset{j}{\mathfrak{R}_i^v}} \end{bmatrix}. \tag{10}$$

$\overset{j}{E}\left[\sqrt{r}\right]$ can be expressed in closed form

$$\overset{j}{E}\left[\sqrt{\boldsymbol{r}}\right] = \frac{\int_{R_j^{in}}^{R_j^{out}} 2\pi \boldsymbol{r}\sqrt{\boldsymbol{r}}d\boldsymbol{r}}{\int_{R_j^{in}}^{R_j^{out}} 2\pi \boldsymbol{r}d\boldsymbol{r}} = \frac{4}{5}\sqrt{R_j^{out}}\frac{1-\alpha^{-5/2}}{1-\alpha^{-2}}, \tag{11}$$

where the outer radius of the sub-annulus j is defined as $R_j^{out} = \alpha R_j^{in}$. Equation (10) can then be understood to equate the average observed value of displacement components to the radius of the sub-annulus with a single constant that is independent of crack orientation, K_I, K_{II}, and elastic properties of the material, i.e.

$$\overline{\overset{j}{u_i^{obs}}} = C_1\sqrt{R_j^{out}} + \overline{\overset{j}{\mathfrak{R}_i^u}} \tag{12}$$

and

$$\overline{\overset{j}{v_i^{obs}}} = C_2\sqrt{R_j^{out}} + \overline{\overset{j}{\mathfrak{R}_i^v}}\,. \tag{13}$$

Similar to Equation (5), the discrepancy between the average observed value of displacement components at a given data point i and the product of the constant with the square root of the outer radius of the sub-annulus j, is quantified with a residual vector

$$\begin{bmatrix} \overline{\overset{j}{\mathfrak{R}_i^u}} \\ \overline{\overset{j}{\mathfrak{R}_i^v}} \end{bmatrix} = \begin{bmatrix} \overline{\overset{j}{u_i^{obs}}} - C_1\sqrt{R_j^{out}} \\ \overline{\overset{j}{v_i^{obs}}} - C_2\sqrt{R_j^{out}} \end{bmatrix}. \tag{14}$$

Given values of $\overline{\overset{j}{u_i^{obs}}}$ and $\overline{\overset{j}{v_i^{obs}}}$ for each sub-annulus j, the values of the constants C_1 and C_2 that minimize the normalized length of the residual vector across all m sub-annuli that partition the annulus give the best fit LEFM model via a least squares measure,

$$\Phi^{sep} = \frac{1}{m}\sum_{j=0}^{m}\left(\left(\overline{\overset{j}{\mathfrak{R}_i^u}}\right)^2 + \left(\overline{\overset{j}{\mathfrak{R}_i^v}}\right)^2\right). \tag{15}$$

Equations (6) and (15) are nonlinear equations w.r.t. the unknown parameters. A pattern search optimization algorithm (Diniz-Ehrhardt et al., 2017; Zanganeh et al., 2013) was used to find the minimum of the displacement correlation and separability cost functions.

4 Analysis of Separability and Displacement Correlation Approaches

To assess the utility of the separability approach relative to the existing displacement correlation approach, four attributes are considered: (1) cost function landscape, (2) robustness in application to non-ideal data sets, (3) robustness relative to noise in the data set, and (4) computational expense.

4.1 Cost Function Landscape

Cost function landscapes for the displacement correlation (Equation (6)) and separability (Equation (15)) approaches are presented in Figure 3 for a range of assumed crack tip positions, $\widetilde{x^{tip'}}$ and $\widetilde{y^{tip'}}$. Each row of the figure corresponds to the cost function landscapes for the two approaches associated with a different synthetic data set. The first three rows correspond to displacements generated from Equation (1) using pure mode I, pure mode II, and mixed mode loading with nonzero T-stress. The fourth set mimics the third but includes the addition of an independent and identically distributed Gaussian noise to each component of the data set. The noise had a mean of zero and a standard deviation of $\sigma = 0.025R^{out} = 0.5L$, i.e.

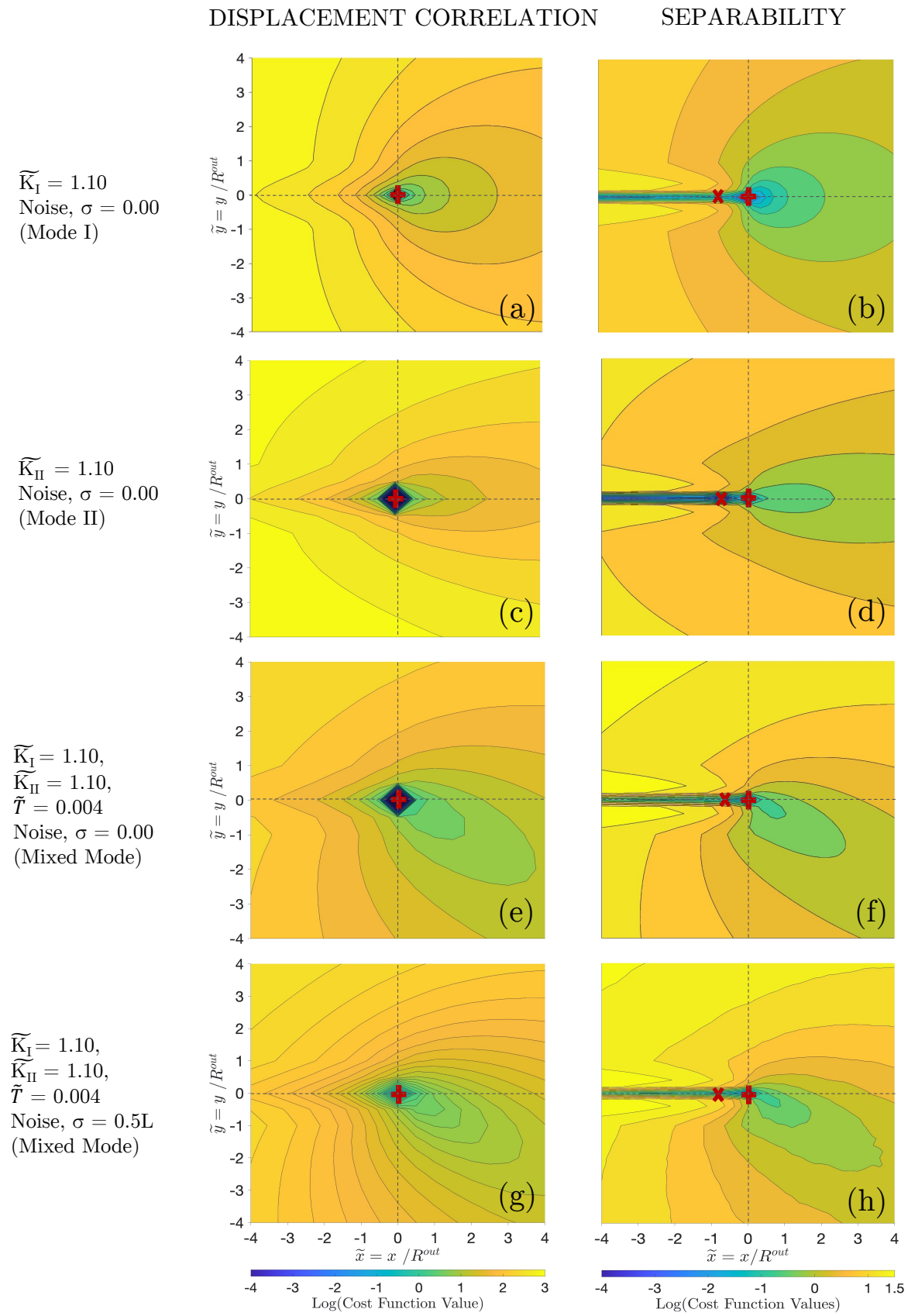

Fig. 3 Comparison of the cost function landscapes of the displacement correlation and separability approaches for (a) - (b) mode I, (c) - (d) mode II and (e) - (f) mixed modes (including T-stress) of fracture in the case of no noise in the data. (g) - (h) Effect of noise on the displacement correlation and separability cost functions in the mixed mode scenario. The value of noise points to the mean of a random displacement of Gaussian distribution. The global minimum value of the respective cost functions, signifying the position of the crack tip inferred by each approach, is represented by the $'+'$ sign in the color maps. The $'X'$ sign signifies the multiple local minima seen in the separability cost function plots.

$\delta_i^u \sim \mathcal{N}(0, \sigma^2)$ and $\delta_i^v \sim \mathcal{N}(0, \sigma^2)$ were added to each component of the data set. For perspective, we note that this noise level is large relative to the molecular dynamics of common structural materials at 300K, which would have noise levels in the range of $\sigma = 0.01L$ to $0.04L$ (Liang and Ye, 2014; Mai and Choi, 2018; Williams, 1957).

For consistency with section 2, the grid and annulus sizes remained $L = 0.05R^{out}$ and $R^{in} = 0.1R^{out}$ respectively, which equated to 1240 points within the annulus. In all cases, the synthetic data set corresponds to a crack tip positioned at (0,0) and having an orientation of 0°. Two sub-annuli were used for the separability approach, i.e. $m = 2$ in Equation (15). Based on the analysis shown in Section 4.3, this value of $m = 2$ minimizes the amount of noise for a given number of points.

As expected from the linearity of LEFM fracture modes, the mixed mode contour landscapes (Figure 3e and f) can be viewed as the sum of mode I and mode II landscapes, plus the influence of a uniform T-stress that acts parallel to the crack face plane. The landscape of the fourth row (which includes noise) does not differ significantly from the third, showing that the addition of this level of noise was nominally inconsequential. With the parameters used, a very large noise level of $\sigma = L$ was required before the effects of noise were substantial in the two approaches. Taking an average over 50 simulations at the noise level of $\sigma = L$, the position error for the displacement correlation approach was 0.16L and for separability, this error in inferred crack tip was 0.20L. Doubling the number of points within the annulus reduced this error to 0.15L for displacement correlation and 0.06L for separability. All landscapes shown in Figure 3 have a global minimum at the true crack tip position and are convex within a distance of R^{out} about that position.

Beyond these similarities, the separability landscapes display some inferior attributes relative to the displacement correlation landscapes. First, the separability landscapes display a roughness, even in the cases where no noise was added to the synthetic data set. This is attributed to the error in computing the expectation in Equation (11) from a finite sized data set. Second, the separability landscape can show multiple minima, whereas the displacement correlation landscape remains convex with a single minimum within the $4R^{out}$ domain examined. If insufficient points are used in the separability method, either due to low point density or insufficiently sized annulus, multiple minimum can appear at multiples of R^{out}. Fortunately, the multiple minima of the separability approach are organized along the crack plane at a spacing of R^{out}, which does reduce their impact on the identification of the crack tip, i.e. the minimization algorithm can be set to expect this specific situation. The occurrence of such local minimum is dependent of the choice of annulus dimensions, both α and R^{out}, and the number of points in the annulus. Third, the separability cost function is flatter, i.e. has less curvature, meaning that it would be more easily disrupted by noise. The effect of this difference with respect to noise is discussed more quantitatively in Section 4.3.

4.2 Robustness in Application to Non-Ideal Data Sets

To assess the robustness of the separability approach, three cases involving data sets that do not correspond to the ideal asymptotic LEFM solution were examined. In all cases, the data sets were generated from non-deal displacements obtained by Finite Element (FE) solutions to boundary value problems. The FE mesh involved two regions, each entailing a uniform grid of six node quadratic triangular elements. The FE solution was obtained by fully integrating the elements with six integration points. Centered at the crack tip was a $3R^{out}$ by $3R^{out}$ region of finer elements with an edge length of $0.05R^{out}$. This finer meshed region was encompassed in a $10R^{out}$ by $10R^{out}$ region of coarser elements with an edge length of $0.1R^{out}$. A crack of length of $5R^{out}$ extended across half of the FE domain.

A Poisson's ratio of 0.28 was assigned, corresponding to a Kolosov constant (= 3 - 4ν) of 1.88 in plane strain. In all cases the symmetry of the problem permitted simulation of only half the domain, mirrored about the crack plane (Figure 4). For the cost function landscapes presented in Figure 4, there were ∼1,260 points within the annulus in the fine mesh region. As the annulus gradually moved outside of the fine mesh region to evaluate the cost function at distances up to $4R^{out}$ away from the crack tip, the number of points

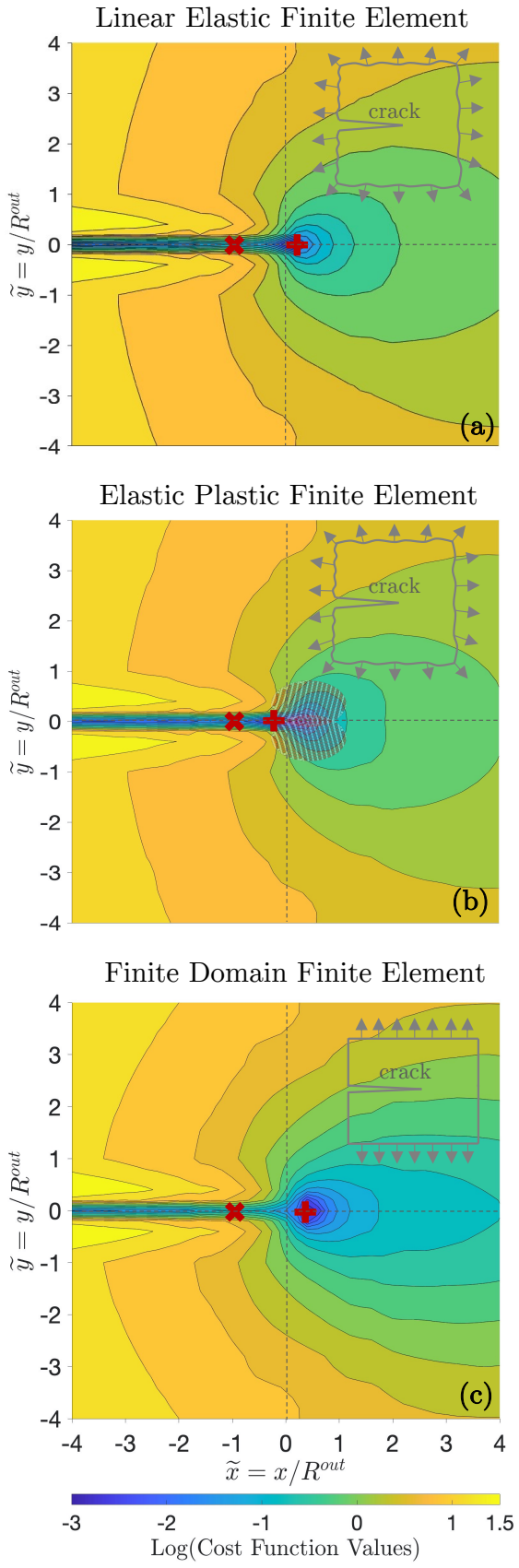

Fig. 4 Separability cost function maps in non-ideal datasets. (a) Linear Elastic Finite Element (b) Elastic Plastic Finite Element, and (c) Linear Elastic Finite Domain Finite Element. The global minimum value of the respective cost functions, signifying the position of the crack tip inferred by each approach, is represented by the $'+'$ sign while the $'X'$ sign demonstrate the presence of the multiple local minima seen. The boundary conditions for each case are shown in grey. Sub-figure (b) also displays the plastic zone in the crack tip region in the elastic-plastic case.

within the annulus reduced. Once the annulus lied entirely in the coarse mesh region, there were ∼300 points within the annulus.

Case I entailed a linear elastic domain with displacement boundary conditions taken from the the LEFM solution for a sharp crack in an infinite isotropic elastic medium (Equation (1)). Specifically, the boundary conditions corresponded to pure mode I loading with $\widetilde{K_I} = 1.10$ and $\widetilde{K_{II}} = \widetilde{T} = 0$. In the domain, the FE displacements differ from the LEFM solution in the region near the crack tip where the quadratic shape functions are incapable of capturing the LEFM solution. Given that the FE solution is stiffer, its displacement magnitudes approaching the crack face are less than the LEFM solution (Hughes, 2012); and thus, the inferred stress intensity factor is less than the far field applied value when providing the correct (0,0) crack tip position (line 2 in Table 1).

With both the displacement correlation and separability approaches, the crack tip position is inferred to be in front of the true position. This is consistent with the discrepancy in displacements between the FE and LEFM solutions being most significant in the region immediately behind the crack tip. As such, the cost functions are minimized at a location ahead of the crack tip. As shown in Figure 2, this error in crack tip position leads to an underpredicted stress intensity factor. Hence, both displacement correlation and separability lead to underpredicted stress intensity factors for this data set due to two distinct causes: the lower displacement magnitudes at the crack tip and the identification of a crack tip position that is in front of the true crack tip.

Case II entailed the same boundary conditions as case I, but involved an elastic-plastic linear hardening J2 plasticity material model with a normal flow rule (Figure 4b). A kinematic hardening modulus of $0.10E$, isotropic hardening of also $0.10E$ and an initial yield strength of $0.12E$ was used. The initial yield strength was chosen so that there was substantial overlap between the plastic zone and the annulus, as can be seen in Figure 4b. The length of the plastic zone along the y axis was $2R^{out}$ for the selected loading and material properties.

The addition of plastic strain to the model increases the displacement magnitudes near the crack tip relative to case I. This equates to an increase in the inferred stress intensity factor relative to case I (line 5 in Table 1). When using displacement correlation to locate the crack tip position, the occurrence of plasticity causes the inferred crack tip position to shift forward, due to the greatest discrepancy in displacements occurring behind the crack tip (comparing elastic-plastic with LEFM case). This shift is consistent with small scale yielding elastic-plastic fracture mechanics (Zehnder, 2012). As depicted in Figure 2, the shift/error in crack tip position decreases the predicted stress intensity factor, counteracting the effect of increased displacement magnitudes. In the case where separability is used to identify the crack tip position, the inferred crack tip is shifted behind the true tip position (Figure 4b), leading to an even greater value of inferred stress intensity factor.

Case III entailed the same linear elastic material model as case I, but different boundary conditions. In this case, the left and right boundaries of the domain were traction free and a constant traction was applied to the top and bottom boundaries (Figure 4c). The magnitude of the applied traction was chosen following the LEFM equations for an edge crack in a finite plate of size $5R^{out}$ by $10R^{out}$ (Tada et al., 1973) such that $\widetilde{K_I} = 1.10$ to enable direct comparison with the previous cases. In total, the FE model of case III produces a displacement field that differs from the asymptotic LEFM solution both close and far from the crack tip. In close range the difference is due to the FE approximation, while at far range the difference is due to the boundary effects of the finite domain.

For a crack tip position at (0,0) in this geometry, a smaller stress intensity factor of 0.92 is inferred (line 10 in Table 1). The difference between this value and that of case I (line 2 in Table 1) can be attributed to the presence of the model domain boundaries and is consistent with the elasticity solution (Tada et al., 1973). When displacement correlation and separability are used to infer the crack tip position, both return a predicted crack tip position that is in front of the true position. We interpret this result to be due to the displacement field being more influenced by the finite domain behind the crack tip, rather than in front of

Table 1 A comparison of separability (sep) and displacement correlation (dc) approaches applied to non-ideal cases: Linear Elastic Fracture Mechanics (LEFM) Finite Element (FE), Elastic Plastic Fracture Mechanics (EPFM) FE and linear elastic Finite Domain FE.

		$\widetilde{K_I}$	$\widetilde{K_{II}}$	$\widetilde{T}$	$\widetilde{x}$	$\widetilde{y}$	**Avg. iterations**	**Avg. time(s)**
1.	Analytic Solution	1.10	0.00	0.00	0.00	0.00	–	–
2.	LEFM FE- given tip	1.03	0.04	0.00	0.00	0.00	–	–
3.	LEFM FE- dc	0.83	-0.01	0.01	0.20	0.02	166	3.43
4.	LEFM FE- sep	0.88	0.03	0.01	0.15	0.00	22	**0.01**
5.	EPFM FE- given tip	1.17	0.05	-0.03	0.00	0.00	–	–
6.	EPFM FE- dc	0.91	-0.01	-0.01	0.25	0.02	148	4.02
7.	EPFM FE- sep	1.38	0.06	-0.04	-0.25	0.00	24	**0.07**
8.	EPFM FE- dc, apt annulus	1.05	-0.02	-0.01	0.08	0.01	362	7.49
9.	EPFM FE- sep, apt annulus	1.13	0.03	-0.01	0.02	0.00	45	**0.25**
10.	Finite Domain FE- given tip	0.92	0.03	-0.02	0.00	0.00	–	–
11.	Finite Domain FE- dc	0.43	0.01	0.00	0.55	0.04	108	3.98
12.	Finite Domain FE- sep	0.49	-0.01	0.00	0.47	-0.03	32	**0.07**
13.	Finite Domain FE- dc, apt annulus	0.64	0.01	-0.01	0.30	0.00	174	3.12
14.	Finite Domain FE- sep, apt annulus	0.75	0.02	0.01	0.18	0.00	34	**0.08**

it. This error in crack tip position further reduces the inferred crack tip stress intensity factor as shown in Table 1.

In all cases, the non-ideal nature of the data did not qualitatively alter the cost function landscape (Figure 4). Quantitatively, the minimum of the separability landscapes (inferred crack tip position) displayed equal or greater accuracy than the displacement correlation landscapes. That said, in the case of crack tip non-linearity, the separability approach produces an error in the opposite direction of the displacement correlation approach. This can have substantial implications on the value of the stress intensity factor that is ultimately inferred. With separability, the error in the crack tip position leads to an error in stress intensity factor. This discrepancy adds to the error associated with the plastic displacements near the crack tip. That said, in practice one should attempt to chose an annulus that is larger than the plastic zone size (Pataky et al., 2012) and significantly smaller than the domain size. In Table 1 and Figure 4, this was not the case.

For illustration, case II was reexamined with R^{out} being twice the plastic zone size. In this scenario, the separability approach infers a stress intensity factors within 1.8% of the values at true crack tip position (0,0). In this setting, the inferred crack tip returned by the separability approach is $(0.02,\ 0.00)R^{out}$. Qualitatively different from lines 6 and 7 in Table 1, these values are more accurate than the values computed with the displacement correlation approach, where the inferred stress intensity factor is 7.50% from the true value and the associated inferred crack tip is $(0.08,\ 0.01)R^{out}$. Thus, the choice of annulus is fundamental to the accuracy of the separability approach.

4.3 Robustness relative to noise in the data set

The sensitivity of the cost functions to random noise in the observed data is a key attribute that controls the utility of the cost functions for inferring crack tip position. The separability approach involves minimization of a cost function with less curvature than displacement correlation (Figure 3), but the separability approach

it is built upon average values of the displacement making it less sensitive to noise when there are sufficient data points to compute the averages precisely.

In the simple case where the observed displacement vector components only differ from the linear elastic model by an independent and identically distributed Gaussian noise of mean zero and standard deviation σ, i.e. $\delta_i^u \sim \mathcal{N}(0, \sigma^2)$ and $\delta_i^v \sim \mathcal{N}(0, \sigma^2)$, Equation (6) takes the form

$$\Phi^{dc} = \frac{1}{n} \sum_{i=0}^{n} \left((\delta_i^u)^2 + (\delta_i^v)^2 \right). \tag{16}$$

In this case, Φ^{dc} is a sampled statistic that follows a Chi-squared distribution with a standard deviation of

$$\text{stdev}(\Phi^{dc}) = 2\sigma^2/\sqrt{n}. \tag{17}$$

The analysis of the separability cost function is more complicated, requiring the distribution of the sampled average displacement components in sub-annuli j to be assessed, $\overline{u_i^{obs}}^j$ and $\overline{v_i^{obs}}^j$. To start, $\overline{u_i^{obs}}^j$ and $\overline{v_i^{obs}}^j$ are written in terms of the expectation of u and v in the LEFM model and in the sub annulus j as

$$\begin{aligned} \overline{u_i^{obs}}^j &= E^j[u] + \epsilon^j[u_i] + \delta_i^u, \\ \overline{v_i^{obs}}^j &= E^j[v] + \epsilon^j[v_i] + \delta_i^v, \end{aligned} \tag{18}$$

with $\epsilon^j[u_i]$ and $\epsilon^j[u_i]$ representing the difference between the sampled average values and the expectation in the absence of noise. In other words, $\epsilon^j[u_i]$ and $\epsilon^j[u_i]$ represent the residual associated with approximating the integral in the expectation operator with Monte Carlo Integration.

Plugging Equations (12) and (13) into Equation (18) provides an expression for the residuals given sampled data points within an annulus j,

$$\begin{aligned} \overline{\mathfrak{R}_i^u}^j &= C_1(K_I, K_{II}, \mu, \kappa, \phi)\sqrt{R_j^{out}} - (E^j[u] + \epsilon^j[u_i] + \delta_i^u), \\ \overline{\mathfrak{R}_i^v}^j &= C_2(K_I, K_{II}, \mu, \kappa, \phi)\sqrt{R_j^{out}} - (E^j[v] + \epsilon^j[v_i] + \delta_i^v). \end{aligned} \tag{19}$$

In the simple case considered previously, where the observed sampling of displacement vector components only differ from the linear elastic model by an independent and identically distributed Gaussian noise of mean zero and standard deviation σ, Equations (19) reduce to

$$\begin{aligned} \overline{\mathfrak{R}_i^u}^j &= -(\epsilon^j[u_i] + \overline{\delta_i^u}), \\ \overline{\mathfrak{R}_i^v}^j &= -(\epsilon^j[v_i] + \overline{\delta_i^v}). \end{aligned} \tag{20}$$

The cost function for the separability approach, Equation (15), reduces to

$$\Phi^{sep} = \frac{1}{m} \sum_{j=0}^{m} \left(\epsilon^j[u_i] + \overline{\delta_i^u} \right)^2 + \left(\epsilon^j[v_i] + \overline{\delta_i^v} \right)^2, \tag{21}$$

Given that $\delta_i^u \sim \mathcal{N}(0, \sigma^2)$, the sampled average of δ_i^u on n/m data points within a sub-annulus is distributed as $\overline{\delta_i^u} \sim \mathcal{N}(0, \sigma^2 m/n)$. Here, n/m data points per sub-annulus are considered to enable a direct

comparison between the displacement correlation and separability approaches when the same number of data points are utilized in both cases.

The distributions of $\overset{j}{\epsilon}[u_i]$ and $\overset{j}{\epsilon}[v_i]$ depend on the distribution of the population from which u_i and v_i are sampled. This depends on $K_I, K_{II}, \mu, \kappa, \phi$. While one could compute it exactly for a specific choice of these parameters, we proceed more generally, approximating it as a uniform distribution from u_{min} to u_{max} within the annulus. u_{max} is the maximum observed displacement component from the linear elastic model, given $K_I, K_{II}, T, \mu, \kappa, \phi, R^{out}$, and u_{min} is taken to be -u_{max}.

With this assumption, $\overset{j}{\epsilon}[u_i]$ follows a Bates distribution with mean zero and standard deviation $u_{max}/\sqrt{3n/m}$. Considering the value of n/m in practice, the Bates distribution can be approximated by a normal distribution, i.e. $\overset{j}{\epsilon}[u_i] \sim \mathcal{N}(0, mu_{max}^2/3n)$ as $n/m \to \infty$. With this approximation and provided $\overset{j}{\epsilon}[u_i]$ and $\overline{\delta_i^u}$ are independent, $\overset{j}{\epsilon}[u_i] + \overline{\delta_i^u} \sim \mathcal{N}(0, mu_{max}^2/3n + \sigma^2 m/n)$. By the same reasoning, $\overset{j}{\epsilon}[v_i] + \overline{\delta_i^v} \sim \mathcal{N}(0, mv_{max}^2/3n + \sigma^2 m/n)$.

In this context, each side of Equation (21) can then be viewed as a sampled statistic following a sum of two Chi-squared distributions. Insight into the scaling of the variability of Φ^{sep} can subsequently be obtained by considering the simplified case when u_{max}^2 and v_{max}^2 are equal and $\overset{j}{\epsilon}[u_i]$ and $\overset{j}{\epsilon}[v_i]$ are independent, i.e.

$$\text{stdev}(\Phi^{sep}) = \frac{2\sqrt{m}}{n}(u_{max}^2/3 + \sigma^2). \tag{22}$$

A direct comparison of stdev(Φ^{sep}) and stdev(Φ^{dc}) does not provide a fair comparison of the ability of the separability and displacement correlation methods to handle noisy data sets, as the landscape of Φ^{sep} has less curvature. From Figure 3, a factor of 100 can be seen to provide a reasonable approximation of the curvature difference. Therefore, with respect to finding a crack tip in a noisy data set, separability would favorable when 100stdev(Φ^{sep}) < stdev(Φ^{dc}). Utilizing Equations (17) and (22) then gives an approximate inequality between an effective signal-to-noise ratio and the number of points in the data set, giving an indication of when separability would be favorable

$$\frac{u_{max}}{\sigma} < \frac{\sqrt{3}}{10}\sqrt{\sqrt{\frac{n}{m}} - 1} \tag{23}$$

Acknowledging that the separability approach performs best with two sub-annuli, i.e. $m = 2$, Equation (23) suggests separability to be favorable at signal-to-noise ratios ($\frac{u_{max}}{\sigma}$) below 0.2, 0.4, 0.8, and 1.4 for 10, 100, 1000, and 10,000 data points, respectively. With that said, we point out that u_{max} is not just a function of the stress intensity and elastic modulus, but also a function of the annulus size, increasing linearly with $\sqrt{R^{out}}$. Therefore, the signal-to-noise ratio sufficient to motivate the use of the separability approach depends on the annulus size, such that the separability approach is favored at smaller annulus sizes, which are motivated in practice by a desire to limit finite domain effects in the data set.

4.4 Computational expense

The utility of the separability approach depends not only on its robustness when using noisy non-ideal data sets, but also on its computational expense.

The computational expense of the separability cost function (Equation (15)) in the practical case of $n/m \gg 1$ is dominated by the computation of the average displacement components in the sub-annuli. This requires $2n$ additions. The other computations scale with m and m^2 and are thus insignificant when $n/m \gg 1$.

The evaluation of the displacement correlation cost function (Equation (6)) requires significantly more computation, i.e. n square roots, $4n$ trigonometric operations, $12n$ multiplications, and $6n$ addition operations. Further, the cost function must be evaluated more times with the displacement correlation approach, as it involves minimization in a 6D parameter space, whereas the separability cost function is minimized in a 2D parameter space.

Table 1 demonstrates the significant difference in computation time and number of iterations for the two approaches considering the non-ideal data sets that were discussed in section 4.2. In the cases shown, a pattern search optimization algorithm was used to find the minimums of the cost functions (Zanganeh et al., 2013), and n varied between ∼300 and ∼1260 depending upon whether the trial crack tip position was in the fine or coarse meshed regions. A starting guess of ($R^{out}/2$, $R^{out}/2$) was used for all cases. In this context, the computational time of the separability approach is shown to be approximately 30× superior to the displacement correlation approach and is the result of both fewer iterations to solution and less computational time per iteration.

This difference in computational expense means that Equation (23) is not a sufficient indicator in the decision of whether to use the separability approach. For equal computational cost, $\sim 30\times$ points can be used with the separability approach, i.e. $n_{\text{sep}} = 30n_{\text{dc}}$, and therefore following Equation (24) and utilizing the approximations $30\sqrt{n_{\text{dc}}/m} - 1 \approx 30\sqrt{n_{\text{dc}}/m}$ and $\sqrt{90}/10 \approx 1$, the separability approach can be considered favorable when

$$\frac{u_{max}}{\sigma} < \left(\frac{n_{\text{dc}}}{m}\right)^{1/4}. \tag{24}$$

Acknowledging again that the separability approach performs best with two sub-annuli, i.e. $m = 2$, Equation (23) suggests separability to be favorable at signal-to-noise ratios ($\frac{u_{max}}{\sigma}$) below 1.5, 2.7, 4.7, and 8.4 for 10, 100, 1000, and 10,000 data points, respectively, considering the computational costs observed in table 1. Finally, we note that the storage requirements of the separability and displacement correlation approaches are both minimal, as neither scales with n (Wilson et al., 2019).

5 Demonstrations

The separability approach presented in this manuscript has wide-ranging applications. It can be utilized on any displacement dataset that encapsulates a crack tip, from computer simulation and laboratory experiment to field data. The wide applicability is demonstrated in this section by extending beyond the finite element datasets analyzed in the previous section, considering Molecular Dynamics (MD) and Digital Image Correlation (DIC) datasets as two examples.

The MD simulation data presented in Wilson et al. (2019) was used an an example upon which to utilize the separability approach to infer crack tip position. The Wilson et al. data was generated using the Large-scale Atomic/Molecular Massively Parallel Simulator (LAMMPS) (Plimpton, 1995; Thompson et al., 2021) and involved the fracture of a silica glass sample subjected to a uniaxial strain in the y direction with an initial edge crack extending in the x direction that was subjected to mode I loading. The sample was 55x22x5 nm and consisted of 362 thousand atoms at 300K. In the z through crack direction, the specimen was simulated as infinitely thick via periodic boundary conditions. With the uniaxial strain held fixed at a sufficiently high value, the molecular dynamics simulation resulted in crack propagation, with the atomic configurations being analyzed every 400,000 time steps. The separability approach was used to infer the crack tip position at each timestep, with $R^{out} = 62.5$ Å and $\alpha = 2.5$ that yielded $n \approx 29,000$ in this case. Here, the elastic properties of the material were known and could be used to also compute the stress intensity factors associated with the inferred crack tips. In other atomistic fracture simulations where the elastic properties are unknown, the separability approach can still be used to infer crack tip positions without calculating the driving force values.

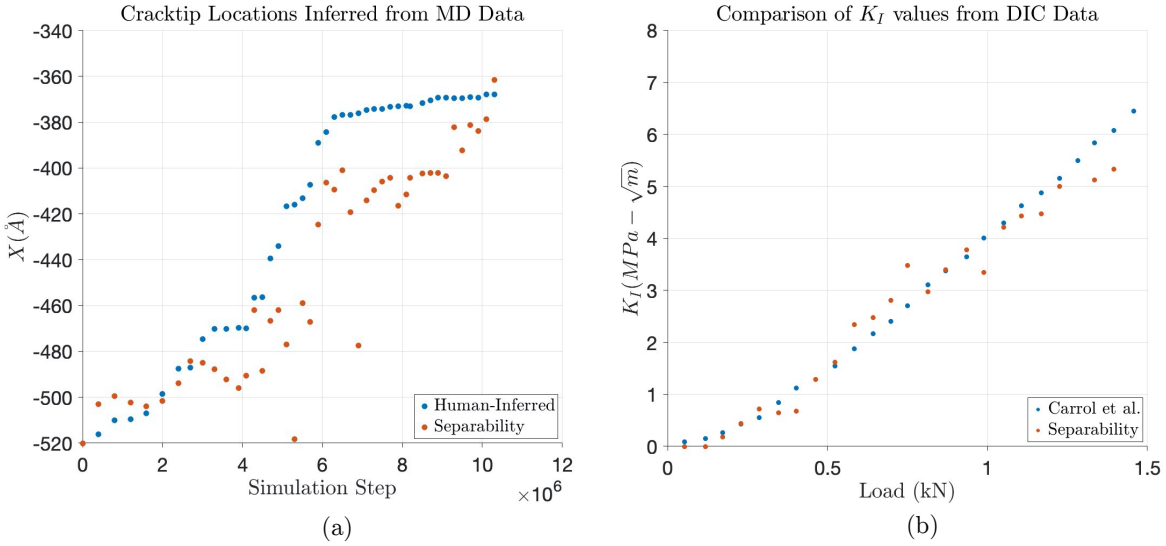

Fig. 5 Applications (a) Comparison of crack tip locations calculated by Separability with the crack tips inferred from MD data. (b) Comparison of K1 values from the Separability with DIC data shown in Figure 12a in the paper by Carroll et al. (2009)

The results of the separability approach across sequential atomic configurations have been compared to the crack positions inferred by visually examining the geometry of the configurations. The degree of correspondence between the two approaches is shown in Figure 5(a). Human inference based upon the geometry of the configurations can be seen to mostly overpredict the length of the crack relative to the separability approach. This over prediction is attributed to the crack tip blunting that occurred in the simulations, which moves the crack tip position defined by LEFM forward relative to the geometrically observable tip position. From Figure 2, this implies that the inferred stress intensity factor from a human inferred crack tip position would be an over prediction of the true value. For engineering applications where simulation data of K_I vs crack velocity might be used to infer material behavior, the error is not conservative. Had sufficient bridging behind the crack occurred, the opposite result would be expected.

The data presented in Carroll et al. (2009) was used as an example to demonstrate the utility of the separability approach to infer crack tip position and ultimately stress intensity factors from DIC experiments. Carroll et al.'s experiments consisted of cyclically loaded single edge-notched tension specimens of commercially pure titanium. A 2-8Hz cyclic loading was performed such that K_{max} was maintained at 19 MPa$\sqrt{\text{m}}$ with a load ratio of nearly zero. Periodically, the cyclic loading rate was slowed to 0.004 Hz to measure the stress intensity factor during the load cycle via DIC. The slower cycle allowed 120 images to be captured throughout the loading cycle. Figure 5(b) gives the inferred K_I values during one of these measurement cycles (as given in Figure 12a in Carroll et al. (2009)), using 5,600 displacement points captured in a 710 X 40 micron field of view surrounding the crack tip. The values of K_I obtained by Carroll et al. were calculated using the displacement correlation technique on the displacement vector in the direction normal to the crack plane and using a crack tip position that was human inferred from the geometry visible using 28x optical microscopy. Carroll et al. excluded a region of 80µm around the crack tip from the displacement correlation data set to exclude the plastic zone.

Inferred K_I values from the separability method applied to this data set are also shown in Figure 5(b). These K_I values were obtained using $R^{out} = 108$µm and $\alpha \approx 2.2$, which yielded $n \approx 140$. The results from

both approaches are found to be similar, although the separability inferred K_I value was more noisy. This noise can be attributed to a large signal to noise ratio for the governing parameters as developed in section 4.3. This leads to a noise in the inferred crack tip position and ultimately in the inferred K_I value as presented in Figure 2. Increasing the annulus size would improve the performance.

6 Conclusions

The occurrence and prevention of fracture has been estimated to consume 4% of the US GDP (Reed, 1983). In attempts to reduce this burden, quantifying the configurational driving force acting on the crack is often paramount. Identifying the crack tip position is a required step toward this goal.

This manuscript has presented a new approach to identify crack tip position from displacement data. The new approach, which we refer to as the separability approach, is particularly useful in cases involving noisy displacement data, where many data points are needed to obtain sufficiently accurate results. Such cases are becoming more prevalent with the increased digitization of the physical world, e.g. digital imaging of laboratory and field data. Further, there are multiple simulation approaches that are used to study fracture that often involve noisy data, such as molecular dynamics at the nanoscale (Zhao et al., 2022) and discrete element and peridynamics at the continuum scale (Baker and Warner, 2012; Stenström and Eriksson, 2019; Wang et al., 2020). In all of the mentioned cases, crack blunting (Gu and Warner, 2021), bridging (Wilson et al., 2019), and microcracking Buehler et al. (2006) can create an inconsistency between geometric approaches to locate crack tip position and the mechanically defined position needed to accurately identify the driving force.

When the dataset is ideal, i.e. in accord with asymptotic linear elastic fracture mechanics, the separability approach will produce a similar result as the widely used displacement correlation approach. Therefore, the appeal of the newly presented separability approach is that it offers computational expediency over the existing approach. This expediency results not only from its time to solution, but also from its ability to produce more accurate solutions from large noisy data sets, enabling the use of smaller displacement data sets in some contexts with the separability approach.

The effect of deviations in the data set from the asymptotic linear elastic ideal, e.g. finite boundary effects and non-linearity near the crack tip, is shown to not be substantially different between the two approaches. In all examined cases, the user of the separability approach should be aware of the potential for multiple local minimal behind the ideal crack tip location, if the choice of annulus dimensions is inappropriate or the number of points in the annulus is insufficient. Nonetheless, the challenge of multiple minimum can easily be addressed within the minimization routine, especially given the computational expediency of the separability approach. In addition to its efficiency, another major advantage of the separability approach is its ability to infer the crack tip location without knowing any elastic constants. This makes separability a particularly valuable approach for those studying atomistic fracture.

A generally applicable python implementation of the separability approach is given at X, and an example involving its utilization within a python wrapper that also calls LAMMPS is given at X.

Acknowledgements

The authors thank J. Carroll for providing displacement and DIC analysis data. The authors thank E. David Reedy for reviewing a draft of the manuscript and providing valuable technical insight. This work was supported in part by the Advanced Simulation and Computing (ASC) program at Sandia National Laboratories for the U.S. Department of Energy's National Nuclear Security Administration. Sandia National Laboratories is a multi-mission laboratory managed and operated by National Technology and Engineering Solutions of Sandia, LLC., a wholly owned subsidiary of Honeywell International, Inc., for the U.S.

Department of Energy's National Nuclear Security Administration under contract DE-NA0003525. This paper describes objective technical results and analysis. Any subjective views or opinions that might be expressed in the paper do not necessarily represent the views of the U.S. Department of Energy or the United States Government. The United States Government retains and the publisher, by accepting the article for publication, acknowledges that the U.S. Government retains a non-exclusive, paid-up, irrevocable, world-wide license to publish or reproduce the published form of this manuscript, or allow others to do so, for U.S. Government purposes. DHW gratefully acknowledges support from the Office of Naval Research #N000142012484 and the National Science Foundation #1922081.

References

Ayatollahi M, Nejati M (2011) An over-deterministic method for calculation of coefficients of crack tip asymptotic field from finite element analysis. Fatigue & Fracture of Engineering Materials & Structures 34(3):159–176

Baker K, Warner D (2012) Extended timescale atomistic modeling of crack tip behavior in aluminum. Modelling and Simulation in Materials Science and Engineering 20(6):065005

Buehler MJ, Van Duin AC, Goddard III WA (2006) Multiparadigm modeling of dynamical crack propagation in silicon using a reactive force field. Physical review letters 96(9):095505

Carroll J, Efstathiou C, Lambros J, Sehitoglu H, Hauber B, Spottswood S, Chona R (2009) Investigation of fatigue crack closure using multiscale image correlation experiments. Engineering Fracture Mechanics 76

Diniz-Ehrhardt M, Ferreira D, Santos S (2017) Combining pattern search and implicit filtering for solving linearly constrained minimization problems with noisy objective functions

Gu W, Warner DH (2021) Dissolution at a ductile crack tip. Physical Review Letters 127(14):146001

Hughes TJ (2012) The finite element method: linear static and dynamic finite element analysis. Courier Corporation

Liang T, Ye W (2014) An efficient hybrid dsmc/md algorithm for accurate modeling of micro gas flows. Communications in Computational Physics 15(1):246–264

Lim I, Johnston I, Choi S (1992) Comparison between various displacement-based stress intensity factor computation techniques. International Journal of Fracture 58(3):193–210

Mai NT, Choi ST (2018) Atomic-scale mutual integrals for mixed-mode fracture: Abnormal fracture toughness of grain boundaries in graphene. International Journal of Solids and Structures 138:205–216

Pataky GJ, Sangid MD, Sehitoglu H, Hamilton RF, Maier HJ, Sofronis P (2012) Full field measurements of anisotropic stress intensity factor ranges in fatigue. Engineering Fracture Mechanics 94:13–28

Plimpton S (1995) Fast parallel algorithms for short-range molecular dynamics. Journal of Computational Physics 117(1):1–19, DOI 10.1006/jcph.1995.1039

Reed RP (1983) The Economic Effects of Fracture in the United States: A report to NBS by Batelle Columbus Laboratories. US Department of Commerce, National Bureau of Standards

Rice JR (1974) Limitations to the small scale yielding approximation for crack tip plasticity. Journal of the Mechanics and Physics of Solids 22(1):17–26

Sanford RJ, Dally JW (1979) A general method for determining mixed-mode stress intensity factors from isochromatic fringe patterns. Engineering Fracture Mechanics 11(4):621–633

Seitl S, Malíková L, Sobek J, Frantík P, Lopez-Crespo P (2017) Williams expansion-based approximation of the stress field in an al 2024 body with a crack from optical measurements. Frattura ed Integrità Strutturale 11(41):323–331

Smith D, Ayatollahi M, Pavier M (2001) The role of t-stress in brittle fracture for linear elastic materials under mixed-mode loading. Fatigue & Fracture of Engineering Materials & Structures 24(2):137–150

Stenström C, Eriksson K (2019) The j-contour integral in peridynamics via displacements. International Journal of Fracture 216(2):173–183

Stepanova L, Roslyakov P (2016) Complete williams asymptotic expansion of the stress field near the crack tip: Analytical solutions, interference-optic methods and numerical experiments. In: AIP Conference Proceedings, AIP Publishing LLC, vol 1785, p 030029

Suresh S (1998) Fatigue of materials. Cambridge university press

Tada H, Paris PC, Irwin GR (1973) The stress analysis of cracks. Handbook, Del Research Corporation 34(1973)

Thompson AP, Aktulga HM, Berger R, Bolintineanu DS, Michael Brown W, Crozier PS, in 't Veld PJ, Kohlmeyer A, Moore SG, Nguyen TD, Shan R, Stevens M, Tranchida J, Trott C, Plimpton SJ (2021) LAMMPS - A flexible simulation tool for particle-based materials modeling at the atomic, meso, and continuum scales. Computer Physics Communications 271:108171, DOI 10.1016/j.cpc.2021.108171, URL https://doi.org/10.1016/j.cpc.2021.108171

Wang B, Oterkus S, Oterkus E (2020) Determination of horizon size in state-based peridynamics. Continuum Mechanics and Thermodynamics pp 1–24

Williams ML (1957) On the stress distribution at the base of a stationary crack

Wilson MA, Grutzik SJ, Chandross M (2019) Continuum stress intensity factors from atomistic fracture simulations. Computer Methods in Applied Mechanics and Engineering 354

Zanganeh M, Lopez-Crespo P, Tai Y, Yates J (2013) Locating the crack tip using displacement field data: a comparative study. Strain 49(2):102–115

Zehnder AT (2012) Fracture mechanics, vol 62. Springer Science & Business Media

Zhao M, Gu W, Warner DH (2022) Atomic mechanism of near threshold fatigue crack growth in vacuum. Nature Communications 13(1):812